



# *Spitzer* Microlensing Parallax for OGLE-2017-BLG-0896 Reveals a Counter-rotating Low-mass Brown Dwarf

Yossi Shvartzvald<sup>1</sup> , Jennifer C. Yee<sup>2</sup> , Jan Skowron<sup>3</sup> , Chung-Uk Lee<sup>4,5</sup> , Andrzej Udalski<sup>3</sup> , Sebastiano Calchi Novati<sup>1</sup> , Valerio Bozza<sup>6,7</sup> , Charles A. Beichman<sup>1</sup> , Geoffrey Bryden<sup>8</sup> , Sean Carey<sup>1</sup> , B. Scott Gaudi<sup>9</sup> , Calen B. Henderson<sup>1</sup> , Wei Zhu<sup>10</sup>

(*Spitzer* team),

Etienne Bachelet<sup>11</sup> , Greg Bolt<sup>12</sup> , Grant Christie<sup>13</sup> , Dan Maoz<sup>14</sup> , Tim Natusch<sup>13,15</sup> , Richard W. Pogge<sup>9</sup> , Rachel A. Street<sup>11</sup> , Thiam-Guan Tan<sup>16</sup> , Yiannis Tsapras<sup>17</sup>

(LCO and  $\mu$ FUN Follow-up Teams),

Paweł Pietrukowicz<sup>3</sup> , Igor Soszyński<sup>3</sup> , Michał K. Szymański<sup>3</sup> , Przemek Mróz<sup>3</sup> , Radosław Poleski<sup>3,9</sup> , Szymon Kozłowski<sup>3</sup> , Krzysztof Ulaczyk<sup>3</sup> , Michał Pawlak<sup>3</sup> , Krzysztof A. Rybicki<sup>3</sup> , Patryk Iwanek<sup>3</sup>

(OGLE Collaboration),

Michael D. Albrow<sup>18</sup> , Sang-Mok Cha<sup>4,19</sup> , Sun-Ju Chung<sup>4,5</sup> , Andrew Gould<sup>4,9,20</sup> , Cheongho Han<sup>21</sup> , Kyu-Ha Hwang<sup>4</sup> , Youn Kil Jung<sup>2,4</sup> , Dong-Jin Kim<sup>4</sup> , Hyoun-Woo Kim<sup>4</sup> , Seung-Lee Kim<sup>4,5</sup> , Dong-Joo Lee<sup>4</sup> , Yongseok Lee<sup>4,19</sup> , Byeong-Gon Park<sup>4,5</sup> , Yoon-Hyun Ryu<sup>4</sup> , In-Gu Shin<sup>2</sup> , Weicheng Zang<sup>22,23</sup>

(KMTNet Collaboration),  
and

Martin Dominik<sup>24</sup> , Christiane Helling<sup>24</sup> , Markus Hundertmark<sup>17</sup> , Uffe G. Jørgensen<sup>25</sup> , Penelope Longa-Peña<sup>26</sup> , Stephen Lowry<sup>27</sup> , Sedighe Sajadian<sup>28</sup> , Martin J. Burgdorf<sup>29</sup> , Justyn Campbell-White<sup>27</sup> , Simona Ciceri<sup>30</sup> , Daniel F. Evans<sup>31</sup> , Yuri I. Fujii<sup>25,32,33</sup> , Tobias C. Hinse<sup>4</sup> , Sohrab Rahvar<sup>34</sup> , Markus Rabus<sup>20,35</sup> , Jesper Skottfelt<sup>25,36</sup> , Colin Snodgrass<sup>36</sup> , and John Southworth<sup>31</sup>

(MiNSTEp Collaboration)

<sup>1</sup> IPAC, Mail Code 100-22, Caltech, 1200 E. California Boulevard, Pasadena, CA 91125, USA; [yossishv@gmail.com](mailto:yossishv@gmail.com)

<sup>2</sup> Harvard-Smithsonian Center for Astrophysics, 60 Garden Street, Cambridge, MA 02138, USA

<sup>3</sup> Warsaw University Observatory, Al. Ujazdowskie 4, 00-478 Warszawa, Poland

<sup>4</sup> Korea Astronomy and Space Science Institute, Daejeon 34055, Republic of Korea

<sup>5</sup> Korea University of Science and Technology, 217 Gajeong-ro, Yuseong-gu, Daejeon 34113, Republic of Korea

<sup>6</sup> Dipartimento di Fisica “E.R. Caianiello,” Università di Salerno, Via Giovanni Paolo II 132, I-84084, Fisciano, Italy

<sup>7</sup> Istituto Nazionale di Fisica Nucleare, Sezione di Napoli, Napoli, Italy

<sup>8</sup> Jet Propulsion Laboratory, California Institute of Technology, 4800 Oak Grove Drive, Pasadena, CA 91109, USA

<sup>9</sup> Department of Astronomy, Ohio State University, 140 W. 18th Avenue, Columbus, OH 43210, USA

<sup>10</sup> Canadian Institute for Theoretical Astrophysics, University of Toronto, 60 St. George Street, Toronto, ON M5S 3H8, Canada

<sup>11</sup> Las Cumbres Observatory, 6740 Cortona Drive, suite 102, Goleta, CA 93117, USA

<sup>12</sup> Craigie, Western Australia, Australia

<sup>13</sup> Auckland Observatory, Auckland, New Zealand

<sup>14</sup> School of Physics and Astronomy, Tel-Aviv University, Tel-Aviv 6997801, Israel

<sup>15</sup> Institute for Radio Astronomy and Space Research (IRASR), AUT University, Auckland, New Zealand

<sup>16</sup> Perth Exoplanet Survey Telescope, Perth, Australia

<sup>17</sup> Astronomisches Rechen-Institut, Zentrum für Astronomie der Universität Heidelberg (ZAH), D-69120 Heidelberg, Germany

<sup>18</sup> University of Canterbury, Department of Physics and Astronomy, Private Bag 4800, Christchurch 8020, New Zealand

<sup>19</sup> School of Space Research, Kyung Hee University, Yongin, Gyeonggi 17104, Republic of Korea

<sup>20</sup> Max-Planck-Institute for Astronomy, Königstuhl 17, D-69117 Heidelberg, Germany

<sup>21</sup> Department of Physics, Chungbuk National University, Cheongju 28644, Republic of Korea

<sup>22</sup> Physics Department and Tsinghua Centre for Astrophysics, Tsinghua University, Beijing 100084, People’s Republic of China

<sup>23</sup> Department of Physics, Zhejiang University, Hangzhou, 310058, People’s Republic of China

<sup>24</sup> Centre for Exoplanet Science, SUPA, School of Physics & Astronomy, University of St Andrews, North Haugh, St Andrews KY16 9SS, UK

<sup>25</sup> Niels Bohr Institute & Centre for Star and Planet Formation, University of Copenhagen, Øster Voldgade 5, DK-1350 Copenhagen, Denmark

<sup>26</sup> Unidad de Astronomía, Facultad de Ciencias Básicas, Universidad de Antofagasta, Av. Angamos 601, Antofagasta, Chile

<sup>27</sup> Centre for Astrophysics & Planetary Science, The University of Kent, Canterbury CT2 7NH, UK

<sup>28</sup> Department of Physics, Isfahan University of Technology, Isfahan 84156-83111, Iran

<sup>29</sup> Universität Hamburg, Faculty of Mathematics, Informatics and Natural Sciences, Department of Earth Sciences, Meteorological Institute, Bundesstraße 55, D-20146 Hamburg, Germany

<sup>30</sup> Department of Astronomy, Stockholm University, Alba Nova University Center, SE-106 91, Stockholm, Sweden

<sup>31</sup> Astrophysics Group, Keele University, Staffordshire, ST5 5BG, UK

<sup>32</sup> Institute for Advanced Research, Nagoya University, Furo-cho, Chikusa-ku, Nagoya, 464-8601, Japan

<sup>33</sup> Department of Physics, Nagoya University, Furo-cho, Chikusa-ku, Nagoya 464-8602, Japan

<sup>34</sup> Department of Physics, Sharif University of Technology, P.O. Box 11155-9161, Tehran, Iran

<sup>35</sup> Centro de Astroingeniería, Facultad de Física, Pontificia Universidad Católica de Chile, Av. Vicuña Mackenna 4860, Macul 7820436, Santiago, Chile

<sup>36</sup> School of Physical Sciences, Faculty of Science, Technology, Engineering and Mathematics, The Open University, Walton Hall, Milton Keynes, MK7 6AA, UK

Received 2018 May 22; revised 2019 January 8; accepted 2019 January 10; published 2019 February 11

## Abstract

The kinematics of isolated brown dwarfs in the Galaxy, beyond the solar neighborhood, is virtually unknown. Microlensing has the potential to probe this hidden population, as it can measure both the mass and five of the six phase-space coordinates (all except the radial velocity) even of a dark isolated lens. However, the measurements of both the microlens-parallax and finite-source effects are needed in order to recover the full information. Here, we combine the *Spitzer* satellite parallax measurement with the ground-based light curve, which exhibits strong finite-source effects, of event OGLE-2017-BLG-0896. We find two degenerate solutions for the lens (due to the known satellite-parallax degeneracy), which are consistent with each other except for their proper motion. The lens is an isolated brown dwarf with a mass of either  $18 \pm 1 M_J$  or  $20 \pm 1 M_J$ . This is the lowest isolated-object mass measurement to date, only  $\sim 45\%$  more massive than the theoretical deuterium-fusion boundary at solar metallicity, which is the common definition of a free-floating planet. The brown dwarf is located at either  $3.9 \pm 0.1$  kpc or  $4.1 \pm 0.1$  kpc toward the Galactic bulge, but with proper motion in the opposite direction of disk stars, with one solution suggesting it is moving within the Galactic plane. While it is possibly a halo brown dwarf, it might also represent a different, unknown population.

*Key words:* Galaxy: bulge – gravitational lensing: micro

*Supporting material:* data behind figure

## 1. Introduction

The census, including kinematics, of luminous stars has been rapidly improving over the past decade and has just taken a further quantum leap with the publication of the *Gaia* DR2 data release (Gaia Collaboration et al. 2018). In general, it is usually supposed that low-mass brown dwarfs, which are essentially invisible beyond the immediate solar neighborhood, share the kinematics of “normal” stars. While there are no theoretical arguments against this hypothesis, there is also no observational evidence in its favor.

*Spitzer* microlensing offers a unique opportunity to probe the kinematics of low-mass objects. From 2014 to 2018, *Spitzer* has been observing a total of nearly 1000 microlensing events toward the Galactic bulge (Gould et al. 2013, 2014, 2015a, 2015b, 2016) with the aim of measuring their microlens parallax,  $\pi_E$ ,

$$\pi_E = \frac{\pi_{\text{rel}}}{\theta_E} \frac{\boldsymbol{\mu}_{\text{rel}}}{\mu_{\text{rel}}}; \quad \theta_E = \sqrt{\kappa M \pi_{\text{rel}}};$$

$$\kappa \equiv \frac{4G}{c^2 \text{ au}} \simeq 8.14 \frac{\text{mas}}{M_\odot}, \quad (1)$$

where  $(\pi_{\text{rel}}, \boldsymbol{\mu}_{\text{rel}})$  are the lens-source relative (parallax, proper motion) and  $M$  is the mass of the lens. For special cases in which the angular Einstein radius  $\theta_E$  is measured, the *Spitzer* measurement of  $\pi_E$  then yields  $M$  and  $(\pi_{\text{rel}}, \boldsymbol{\mu}_{\text{rel}})$ .

$$M_l = \frac{\theta_E}{\kappa \pi_E}; \quad \pi_{\text{rel}} = \theta_E \pi_E; \quad \boldsymbol{\mu}_{\text{rel}} = \frac{\theta_E}{t_E} \frac{\boldsymbol{\pi}_E}{\pi_E}, \quad (2)$$

where  $t_E$  is the Einstein timescale of the microlensing event. Then, if the source parallax  $\pi_s$  and proper motion  $\boldsymbol{\mu}_s$  are independently measured, one can infer five of the six phase-space coordinates of the lens (even if it is dark), i.e., its position on the sky and

$$\boldsymbol{\pi}_l = \boldsymbol{\pi}_{\text{rel}} + \boldsymbol{\pi}_s; \quad \boldsymbol{\mu}_l = \boldsymbol{\mu}_{\text{rel}} + \boldsymbol{\mu}_s. \quad (3)$$

The key additional step (assuming that  $\pi_E$  is measured) is to measure  $\theta_E$ . For luminous lenses, this can in principle be done by waiting until the lens is well separated from the source, when they can be separately imaged. In this case, their observed separation  $\Delta\theta$  immediately gives  $\boldsymbol{\mu}_{\text{rel}} = \Delta\theta/\Delta t$ , where  $\Delta t$  is the elapsed time since the event. To date such measurements are relatively rare (Alcock et al. 2001; Batista et al. 2015; Bennett et al. 2015)

because one must wait more than 10 yr for typical events to separate, but with next generation (“30 m”) telescopes, they are likely to become routine.

However, for dark lenses, there are only two known methods to measure  $\theta_E$ : astrometric microlensing (Hog et al. 1995; Miyamoto & Yoshii 1995; Walker 1995) and finite-source effects (Gould 1994a). Astrometric microlensing is not generally well-suited to low-mass lenses because their  $\theta_E$  are small.<sup>37</sup> Moreover, while it is a potentially powerful approach for high-mass lenses (e.g., Gould & Yee 2014), it can only be applied to a tiny handful of events with current instruments. This implies that measuring finite-source effects (together with microlens parallaxes) is presently the only viable method to acquire a sample of low-mass dark lenses with measured kinematics.

*Spitzer* microlensing is providing a steady stream of isolated-object mass measurements that is strongly biased toward both low-mass lenses and bright sources. The latter enable relatively easy measurements of  $\boldsymbol{\mu}_s$ , while  $\pi_s$  is reasonably well known for essentially all microlensing events. With these quantities one can apply Equations (2) and (3) to obtain the lens kinematics.

Finite-source effects (i.e., deviations in the light curve relative to the predictions for a point source) occur when a source transits a caustic in the magnification structure (or comes very close to a cusp). This occurs relatively frequently for binary and planetary events because the binary caustic structures are relatively large while the events are usually recognized as planetary in nature because the source passes over or very near a caustic. However, for isolated lenses, the “caustic” consists of a single point, i.e., directly behind the lens itself. Thus, the probability of such a caustic passage (given that there is a microlensing event) is

$$P = \rho \equiv \frac{\theta_*}{\theta_E}, \quad (4)$$

where  $\theta_*$  is the source angular size. This simple equation has two very important implications. First, it means that the rate  $\Gamma_{\text{FS}} = \rho \Gamma_{\mu\text{lens}}$  of events with finite-source effects does not depend on the mass of some class of lenses, but only on their

<sup>37</sup> The angular Einstein radius of a  $0.05 M_\odot$  BD at 4 kpc is  $\theta_E = 0.23$  mas. Thus, its maximal astrometric shift is only  $\delta\theta_c \approx 0.35\theta_E \approx 0.09$  mas.

number density  $n$  (Gould & Yee 2012). That is, while the microlensing rate  $\Gamma_{\mu\text{lens}} \propto n\mu_{\text{rel}}\theta_{\text{E}}$  increases with mass as  $\Gamma_{\mu\text{lens}} \propto M^{1/2}$ , the finite-source rate

$$\Gamma_{\text{FS}} = \rho\Gamma_{\mu\text{lens}} \propto n\mu_{\text{rel}}\theta_*$$
 (5)

does not. Thus, there is a strong bias toward the more common low-mass objects (Kroupa 2001; Chabrier 2003). Second, because (from Equation (5))  $\Gamma_{\text{FS}} \propto \theta_*$ , finite-source effects are strongly biased toward large (hence, bright) stars.

There are four published isolated-object mass measurements from *Spitzer* microlensing in 2015 and 2016 (Zhu et al. 2016; Chung et al. 2017; Shin et al. 2018), and four more that we have identified from *Spitzer* microlensing in 2017. These have masses in ascending order,  $M = (19, 45, 58^\dagger, 80, 88, 235^\dagger, 520, 570^\dagger)M_{\text{Jup}}$ , which illustrates the strong bias toward low-mass objects. Here the “ $\dagger$ ” symbol indicates preliminary estimates for not-yet-published events. Their source radii are (resorted in ascending order)  $\theta_* = (1.4, 5.7, 5.8, 6.0^\dagger, 6.3, 6.8^\dagger, 7.8, 33.7^\dagger) \mu\text{as}$ , which should be compared to  $\theta_* \sim 0.5 \mu\text{as}$  for typical microlensing events.

Here we present the first of the 2017 *Spitzer* isolated-object microlensing mass measurements, OGLE-2017-BLG-0896L. As we will report, it has  $M \simeq 19 M_{\text{J}}$ , making it the lowest-mass object of the sample of eight that have been measured to date. Indeed, this was the initial focus of our interest. However, in the course of checking our results, we noted that the values of  $(\pi_{\text{rel}}, \mu_{\text{rel}})$ , which are automatically returned as part of the mass derivation, pointed to a possible conflict with the known kinematic characteristics of the major populations of the Galaxy. Because this discrepancy could be resolved if the source had mildly unusual characteristics, we undertook the additional step of measuring the source proper motion  $\mu_s$ . Contrary to our expectation, this measurement made the conflict substantially worse. Of course, one cannot draw very strong conclusions from a single unusual object. However, as we note, there are at least some indications that this object may be a member of a previously unrecognized population. We discuss this possibility, as well as possible biases of the *Spitzer* program favoring the detections of such objects, in Section 6.

## 2. Observations

OGLE-2017-BLG-0896 is at (R.A., decl.)<sub>J2000</sub> = (17:39:30.98,  $-27:17:51.1$ ) corresponding to  $(l, b) = (0^\circ69, 2^\circ01)$ . It was discovered and announced as a probable microlensing event by the OGLE Early Warning System (Udalski et al. 1994; Udalski 2003) at UT 20:23 on 2017 May 25. The event lies in OGLE field BLG675 (Udalski et al. 2015), for which OGLE observations were at a cadence of one to three obs/night using their 1.3 m telescope at Las Campanas, Chile.

The Korea Microlensing Telescope Network (KMTNet, Kim et al. 2016) observed this field from its three 1.6 m telescopes at CTIO (Chile, KMTC), SAAO (South Africa, KMTC), and SSO (Australia, KMTC), in its field BLG15 with a cadence of 1 obs hr<sup>-1</sup>. It is designated SAO15N0405.007056 in the KMTNet catalog. We exclude for the fit the KMTNet data over the peak of the event, from HJD'  $\equiv$  HJD - 2450000 = 7910 to HJD' = 7912, as the event got too bright and thus the photometry is affected by nonlinearity.

The great majority of these survey observations was carried out in the *I* band with occasional *V*-band observations made solely to determine source colors. All reductions for the light-curve

analysis were conducted using variants of difference image analysis (DIA, Alard & Lupton 1998), specifically Wozniak (2000) and Albrow et al. (2009).

OGLE-2017-BLG-0896 was announced as a *Spitzer* target at UT 09:21 on 2017 June 5 because it was recognized as a relatively high-magnification event  $A_{\text{max}} \gtrsim 20$  and so with good (Gould & Loeb 1992; Abe et al. 2013) or possibly excellent (Griest & Safizadeh 1998) sensitivity to planets. The *Spitzer* observations themselves could not begin until 17 days later, when the event entered the Sun-angle window, which was coincidentally the first epoch of planned observations, beginning UT 15:46 2017 June 22. The *Spitzer* data were reduced using the Calchi Novati et al. (2015b) algorithm for crowded-field photometry.

The *Spitzer* team alerted the event as high-magnification and mobilized intensive follow-up observations, with the aim of detecting and characterizing any planetary signatures. Follow-up observations were carried out using four of the Las Cumbres Observatory (LCO) global network of telescopes in Chile, South Africa, and Australia, with the SDSS-*i'* filter. The Microlensing Follow Up Network ( $\mu\text{FUN}$ ) followed the event using the 1.3 m SMARTS telescope at CTIO (CT13) with *V/I/H*-bands, the 0.4 m telescope at Auckland Observatory (AO) with *R*-band, the 0.3 m Perth Exoplanet Survey Telescope (PEST) at Perth, Western Australia, and the 0.25 m telescope at Craigie, Western Australia (unfiltered). PEST data were excluded from the analysis due to systematics of unknown origin. The MiNDSTeP team followed the event using the Danish 1.54 m telescope hosted at ESO's La Silla observatory in Chile, with a simultaneous two-color instrument (wide visible and red; See Figure 1 of Evans et al. 2016) providing Lucky Imaging photometry (Skottfelt et al. 2015). For the analysis of the event we use only the Danish red-band data. LCO and AO data were reduced using pySIS (Albrow et al. 2009), CT13 and Craigie data were reduced using DoPhot (Schechter et al. 1993), and Danish data were reduced using a modified version of DanDIA (Bramich et al. 2008).

While no planetary anomalies were detected, the follow-up observations were crucial in order to model the finite-source effects that are clearly shown at the peak of the event (see Figure 1) because the KMTNet data over the peak were affected by nonlinearity and OGLE cadence was not sufficient for the characterization.

## 3. Light-curve Analysis

### 3.1. Ground Data Only

The light curve, as seen from Earth, is of a symmetric high-magnification event with clear deviation from a point source microlensing (Figure 1). These features rule out any reasonable binary lens because no anomaly/asymmetry associated with a central caustic is detected (see Section 5.1). The *Spitzer* data cover only the falling tail of the event, thus not constraining the finite-source size. Therefore, we start by modeling the ground-based data alone.

We fit the ground-based light curve using six parameters to describe the geometry of finite-source point-lens microlensing as well as two flux parameters for each data set,  $f_{s,i}, f_{b,i}$  (for the source and possible blend). The geometric parameters are the Paczyński parameters,  $(t_0, u_0, t_{\text{E}})$  (Paczynski 1986), the scaled angular source size  $\rho = \theta_*/\theta_{\text{E}}$ , and the limb-darkening coefficients  $\Gamma_I$  and  $\Gamma_{\text{Danish}}$  (we use a specific coefficient for

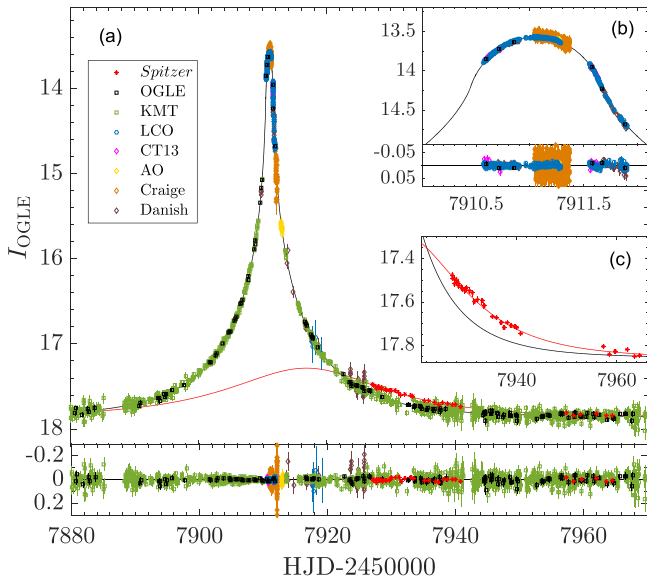


**Figure 1.** Light curve of OGLE-2017-BLG-0896. Finite-source effects are clearly seen at the peak of the event (inset b). The *Spitzer* light curve is significantly offset from the ground-based model (inset c), indicating the large microlens parallax. The data used to create this figure are available.

the Danish data because of the nonstandard filter). We adopt a limb-darkened brightness profile for the source star of the form

$$S_{\lambda}(\phi) = \bar{S}_{\lambda} \left[ 1 - \Gamma_{\lambda} \left( 1 - \frac{3}{2} \cos \phi \right) \right], \quad (6)$$

where  $\bar{S}_{\lambda} \equiv f_{s,\lambda} / (\pi \theta_{*}^2)$  is the mean surface brightness of the source,  $\phi$  is the angle between the normal to the surface of the source star and the line of sight,  $f_{s,\lambda}$  is the total source flux and  $\Gamma_{\lambda}$  is the limb-darkening coefficient at wavelength  $\lambda$ , respectively (An et al. 2002). The limb-darkening coefficients are usually estimated using the source intrinsic properties, which are interpreted from the offset between its observed color and magnitude and the red clump centroid. For this interpretation one assumes that the source is at a similar distance as the clump (i.e., in the bulge). In the case of OGLE-2017-BLG-0896L, the dense coverage during the finite-source effects allows us to well constrain the limb-darkening coefficient,  $\Gamma_I$ , thus enabling us to verify that indeed the source is a bulge star (see Section 4). We use  $\Gamma_I$  and  $\Gamma_{\text{Danish}}$  as free fit parameters, as most of our observations over the peak are with these bands.<sup>38</sup> For AO (*R*-band) and Craige (unfiltered) data, we estimate the limb-darkening coefficient as  $(\Gamma_I + \Gamma_V)/2$ , where  $\Gamma_V = 0.754$  was determined from Claret & Bloemen (2011) based on the characterized source properties (Section 4). The *V*- (OGLE/KMTNet/CT13) and *H*-band (CT13) data are used only to derive the source color, and thus do not require limb-darkening coefficients.

### 3.2. Satellite Parallax Degeneracy

In order to include the *Spitzer* data we add two microlensing parallax parameters,  $\pi_{E,N}$ ,  $\pi_{E,E}$ , aligned with the equatorial north and east directions. Generally, this can introduce the well

known four-fold satellite parallax degeneracy (Refsdal 1966; Gould 1994b). However, because  $|u_{0,\text{ground}}| \ll 1$  the magnitude  $|\pi_E|$  is nearly the same for all solutions (Gould & Yee 2012), and thus the mass and distance of the lensing system are similar. A two-fold degeneracy in the direction of the relative proper motion between the source and the lens persists.

Because *Spitzer* data covered only the falling part of the event and in addition did not fully cover the baseline of the event (see inset of Figure 1), they cannot set strong constraints on  $\pi_E$  by themselves. However, by applying a constraint on the *Spitzer* source flux based on color–color relations, the parallax measurement can be significantly improved (e.g., Calchi Novati et al. 2015a). We derive two color–color relations for OGLE-2017-BLG-0896: a *VIL* relation (using KMTNet data) and an *IHL* relation (using CT13 data), as detailed in Section 4.1. The constraints on *Spitzer* source flux using each of the relations, and consequently the derived parallax values, are in good agreement with each other ( $< 1\sigma$ ). We adopt the *VIL* relation for the final results, because the CT13 data might be subject to low-level chromatic effects.

Table 1 gives the best-fit parameters and their uncertainties for the four-fold degenerate solutions ( $\Delta\chi^2 < 4$ ), which were found using “Newton’s method” (Simpson 1740; see Skowron & Gould 2012). The microlensing parallax components are well constrained, with  $\sim 4\%$  and  $\sim 8\%$  uncertainties on  $\pi_{E,N}$  and  $\pi_{E,E}$ , respectively. These are significantly better than the results without the constraint on *Spitzer* flux, which have 15%–30% uncertainties on the parallax components. It is important to note, however, that the median values are similar. In particular,  $\pi_{E,E} < 0$  at the  $3\sigma$  level even without the color constraint, which is both surprising and interesting as we discuss below in Section 5.

#### 3.2.1. Negative *Spitzer* Blending

The *Spitzer* instrumental blend flux is constrained to be negative when using the color–color relations,  $f_{b,\text{Spitzer}} = -4.4 \pm 1.2$ . While negative blending is known to sometimes be present in ground-based microlensing light curves (e.g., Jiang et al. 2004), its origin in these cases is not always clear. However, for *Spitzer* photometry in crowded fields using the Calchi Novati et al. (2015b) algorithm, the cause for possible artificial negative blending is well understood. As detailed in Calchi Novati et al. (2015b), an input catalog of sources is used to retrieve the *Spitzer* photometry around the event. The catalog is constructed from optical survey data (KMTNet data in the case of OGLE-2017-BLG-0896), which have better resolution and depth than the *Spitzer* image. Any source that is not in the catalog (i.e., unresolved faint stars) will be absorbed in the global background flux, which effectively is subtracted from the source flux, thus resulting as an artificial negative blending. Naturally, this will be more significant in cases for which no real underlying blend in the source position is detected, like in our case ( $f_{b,\text{ogle}} = 0.028 \pm 0.009$ , corresponding to  $5\sigma$  limit of  $I_b > 20.8$ ).

Examining the optical image around the event and comparing it to nearby ( $< 15''$ ) isolated regions, we find an excess of flux due to unresolved stars. The *Spitzer* flux in the isolated regions is significantly lower than the background estimation at the source position. After taking into account the *Spitzer* point-response function, this difference corresponds to  $\sim 5$  flux units of artificial negative blending, which therefore fully explains the negative blend found for *Spitzer*.

<sup>38</sup> We use  $\Gamma_I$  also for LCO SDSS-*i'* data.

**Table 1**  
Microlensing Model

	++	+-	-+	--
$\chi^2$	4126.8	4130.1	4127.0	4130.1
$t_0$ (HJD')	7911.05582(68)	7911.05601(68)	7911.05578(68)	7911.05601(68)
$u_0$	0.0039(11)	0.0037(12)	-0.0038(11)	-0.0037(12)
$t_E$ (day)	14.883(93)	14.896(93)	14.885(93)	14.896(93)
$\rho$	0.04092(31)	0.04085(30)	0.04091(30)	0.04085(31)
$\Gamma_I$	0.525(13)	0.520(13)	0.523(13)	0.522(13)
$\Gamma_{\text{Danish}}$	0.454(23)	0.450(23)	0.453(23)	0.450(23)
$\pi_{\text{EN}}$	-0.779(28)	0.662(29)	-0.771(28)	0.669(29)
$\pi_{\text{EE}}$	-0.615(46)	-0.587(46)	-0.613(46)	-0.589(46)

## 4. Source Star

### 4.1. CMD Analysis and Color–Color Relations

The source photometric properties (color and magnitude) are important for several reasons. First, the source intrinsic properties yield its angular size,  $\theta_*$ , which is needed to derive  $\theta_E$  and the physical properties of the lensing system (Equation (2)). Second, they are used to estimate the limb-darkening coefficients, or alternatively (as in our case) can be compared to the fitted coefficients to verify the estimate of the distance to the source. Lastly, instrumental color–color relations can help constrain the source flux in a third band based on one measured color (e.g., the *Spitzer* *L*-band source flux based on an optical color).

Figure 2 shows the KMTC *V/I* instrumental color–magnitude diagram (CMD) constructed from sources within  $<2'$  of the event. We use the method described in Nataf et al. (2013) to measure the instrumental centroid of the red clump ( $V - I$ ,  $I_{\text{cl,kmt}} = (2.71, 14.18)$ ) and compare it to the intrinsic centroid of ( $V - I$ ,  $I_{\text{cl,0}} = (1.06, 14.41)$ ) (Bensby et al. 2013; Nataf et al. 2013). We determine the instrumental source color from regression of *V* versus *I* flux as the source magnification changes (Gould et al. 2010), and find  $(V - I)_{\text{s,kmt}} = 2.91 \pm 0.03$ . The source instrumental magnitude, as inferred from the microlensing model, is  $I_{\text{s,kmt}} = 14.72 \pm 0.01$ . Assuming that the source lies behind the same dust column as the red clump, its intrinsic properties are  $(V - I, I_{\text{s,0}} = (1.26, 14.95) \pm (0.06, 0.04)$ , accounting also for the red clump instrumental and intrinsic uncertainties. Using standard color–color relations (Bessell & Brett 1988) and the relation between angular source size and surface brightness (Kervella et al. 2004), we find  $\theta_* = 5.71 \pm 0.29 \mu\text{as}$ .

The source position on the CMD, under the assumption that it is a bulge star, suggests a K2.5 III spectral type with  $T_{\text{eff}} \approx 4300$  and  $\log(g) \approx 2.2$ . The corresponding linear limb-darkening coefficients (Claret & Bloemen 2011) are  $\Gamma_I = 0.519 \pm 0.015$  and  $\Gamma_V = 0.754 \pm 0.021$ , where the uncertainties account for a range of possible metallicities and microturbulence velocities. The limb-darkening coefficient  $\Gamma_I$  derived from the fit, for all four degenerate solutions (see Table 1), is within excellent agreement of the estimate based on the source spectral type. This confirms the assumption of a bulge source with similar distance as the red clump. We note that the derived  $\Gamma_I$  can also explain M/K dwarfs. However, these would be either significantly fainter (if in the bulge) or significantly bluer (if nearby).

We extract *Spitzer* photometry for red giant branch stars ( $13.7 < I_{\text{KMT}} < 14.7$ ;  $2.45 < (V - I)_{\text{KMT}} < 2.95$ ), which are a good representation of the bulge giant population, and derive an

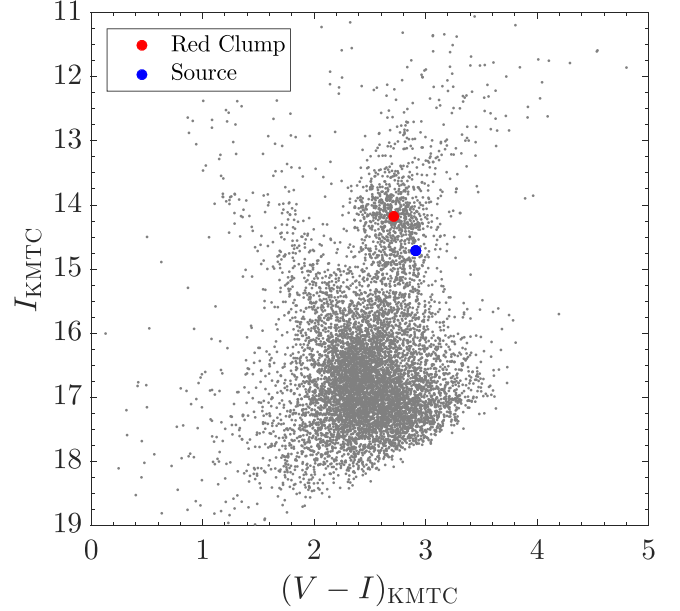


**Figure 2.** KMTC instrumental color–magnitude diagram of OGLE-2017-BLG-0896. The source angular size  $\theta_*$  is derived using the offset between the red clump (red circle) and the source (blue circle) positions.

instrumental *VIL* color–color relation (Calchi Novati et al. 2015b). Applying the relation to the measured  $(V - I)_{\text{s,KMT}}$ , we find  $(I_{\text{KMT}} - L_{\text{Spitzer}})_{\text{s}} = 0.31 \pm 0.05$ . Using this constraint in the microlensing model gives  $f_{\text{s,Spitzer}} = 27.2 \pm 1.2$ . For consistency, we also derive the instrumental *IHL* relation using CT13 data. Applying it to  $(I - H)_{\text{s,CT13}} = 0.53 \pm 0.02$  (derived from regression), we find  $(I_{\text{CT13}} - L_{\text{Spitzer}})_{\text{s}} = 4.45 \pm 0.03$ . This gives  $f_{\text{s,Spitzer}} = 27.0 \pm 0.7$ , in excellent agreement with the constraint using the *VIL* relation. We note that almost all CT13 data (except for three baseline epochs) were taken during the finite-source effects, and thus they might exhibit low-level chromatic effects.

### 4.2. Source Proper Motion

The lens proper motion can be derived from the relative proper motion and the source proper motion (Equation (3)). The source star of OGLE-2017-BLG-0896 is bright, isolated, and has negligible blending (the blend is at least 3 mag fainter), thus permitting a good measurement of its proper motion (unlike most microlensing sources, which are faint and blended). We construct a deep OGLE CMD from a  $6'.5 \times 6'.5$  region centered around the event, and identify

**Table 2**  
Physical Properties

	++	+-	-+	--
$\theta_E$ (mas)	0.1395(72)	0.1398(72)	0.1396(72)	0.1398(72)
$M_l$ ( $M_J$ )	18.1(1.0)	20.3(1.2)	18.2(1.0)	20.2(1.1)
$D_l$ (kpc)	3.86(11)	4.10(12)	3.88(11)	4.08(12)
$\mu_{\text{rel,geo}}$ (mas yr $^{-1}$ )	3.42(18)	3.43(18)	3.42(18)	3.43(18)
$\mu_{l,\text{hel}}(N)$ (mas yr $^{-1}$ )	-7.81(49)	-2.55(50)	-7.80(49)	-2.54(50)
$\mu_{l,\text{hel}}(E)$ (mas yr $^{-1}$ )	-4.43(48)	-4.67(49)	-4.44(48)	-4.65(49)
$v_{l,\text{pec}}(l)$ (km s $^{-1}$ )	-260(10)	-193(10)	-261(10)	-192(10)
$v_{l,\text{pec}}(b)$ (km s $^{-1}$ )	-3(9)	54(10)	-3(9)	54(10)

1527 red clump bulge stars and 730 foreground disk stars. We then use 387 good seeing ( $<1''.35$ ) OGLE epochs from HJD' = 5385–8030 to measure the vector proper motion of each star, with typical uncertainty of  $0.45 \text{ mas yr}^{-1}$  for clump stars. We find that the source proper motion is  $\mu_s(N, E) = (-5.10, -3.15) \pm (0.46, 0.44) \text{ mas yr}^{-1}$  relative to the frame set by the clump giants. Figure 3 shows the source proper motion along with the proper motion distributions of bulge and disk stars. The position of the source on this diagram further supports it being part of the bulge population.

### 5. The Lens: A Counter-rotating Brown Dwarf

The Einstein angular radius is determined by combining  $\rho$  from the model and  $\theta_*$  from the CMD,

$$\theta_E = 0.140 \pm 0.007 \text{ mas.} \quad (7)$$

Combining this with the four degenerate parallax solutions from the microlensing model (Equation (2)) yields a low-mass BD of  $M \simeq 19 M_J$ , with minor differences within  $1\text{--}2\sigma$  between the models (See Table 2). The distance to the BD (Equation (3)) is  $D_l \simeq 4 \text{ kpc}$ , where we assumed  $D_S = 8.3 \text{ kpc}$ , which is appropriate for a bulge source toward the event direction.

The geocentric relative proper motion (Equation (2)) is  $\mu_{\text{rel,geo}} = 3.42 \pm 0.18 \text{ mas yr}^{-1}$ , with either a northwest or a southwest direction as inferred from the parallax components. These already suggest some tension with a disk lens (as would seem to be inferred by  $D_l$ ). In principle, this tension could be resolved if the source had significant northeast proper motion. However, as we found in Section 4.2, the source is actually moving in the opposite direction. Accounting for Earth's projected velocity at the peak of the event,  $V_{\oplus,\pm}(N, E) = (-0.68, 28.9) \text{ km s}^{-1}$ , the two degenerate solutions for the BD heliocentric proper motion relative to the frame set by the bulge clump giants are (see Figure 3),

$$\begin{aligned} \mu_{l,\text{hel}}(N, E) &= \mu_s + (\mu_{\text{rel,geo}} + \pi_{\text{rel}} \mathbf{V}_{\oplus,\pm}) \\ &= \begin{cases} (-7.8, -4.4) \pm (0.5, 0.5) \text{ mas yr}^{-1} \\ \text{or} \\ (-2.5, -4.7) \pm (0.5, 0.5) \text{ mas yr}^{-1}. \end{cases} \end{aligned} \quad (8)$$

In order to find the lens projected velocity, we first note that

$$\begin{aligned} \mu_{l,\text{hel}} &= \mu_s + \mu_{\text{rel,geo}} = \left( \frac{\mathbf{V}_s - \mathbf{V}_\odot}{D_s} - \frac{\mathbf{V}_{\text{cl}} - \mathbf{V}_\odot}{D_{\text{cl}}} \right) \\ &+ \left( \frac{\mathbf{V}_l - \mathbf{V}_\odot}{D_l} - \frac{\mathbf{V}_s - \mathbf{V}_\odot}{D_s} \right), \end{aligned} \quad (9)$$

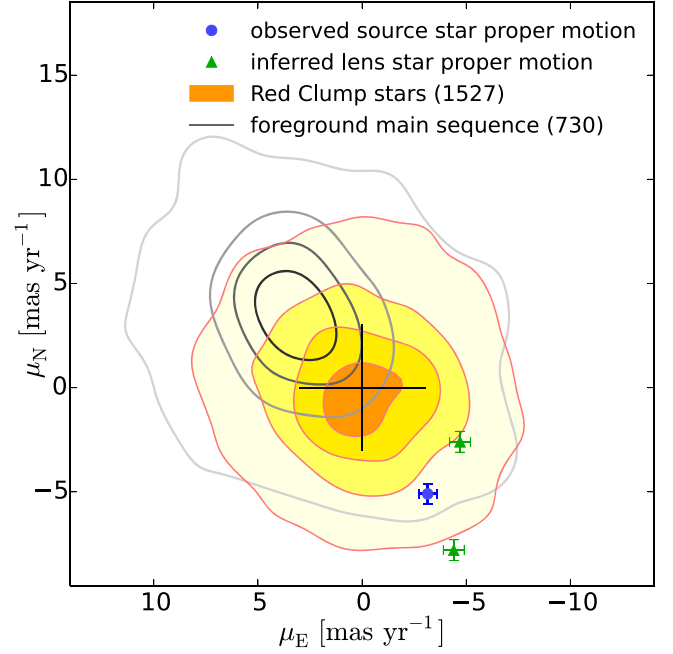


**Figure 3.** OGLE proper motion of bulge (red clump stars) and disk (foreground stars) populations. The contours contain 95.34%, 68.36%, 45.89%, and 24.11% of the stars in each population. We note that the foreground star population represents stars at various distances and thus an effective integration over a range of proper-motion distributions, where nearby stars have the largest proper-motion dispersion. The source observed proper motion (blue circle) and the two degenerate solutions for the lens proper motion (green triangles) are shown.

where  $\mathbf{V}_{\text{cl}}$  and  $D_{\text{cl}}$  are, respectively, the mean velocity and distance of the clump stars that set the proper-motion reference frame. Because the event is at  $l \approx 0$ , we adopt  $V_{\text{cl}}(l, b) = (0, 0) \text{ km s}^{-1}$  and  $D_{\text{cl}} = 8.3 \text{ kpc}$ . The Sun's velocity consists of peculiar velocity,  $V_{\odot,\text{pec}}(l, b) = (12, 7) \text{ km s}^{-1}$  (Schönrich et al. 2010), and the disk circular velocity,  $V_{\text{rot}}(l, b) = (220, 0) \text{ km s}^{-1}$  (Camarillo et al. 2018). Therefore, the two degenerate solutions for the lens peculiar velocity relative to the mean motion disk stars in its neighborhood are

$$\begin{aligned} V_{l,\text{pec}}(l, b) &= \mathbf{V}_l - \mathbf{V}_{\text{rot}} = D_l \mu_{l,\text{hel}} \\ &- \mathbf{V}_{\text{rot}} \left( \frac{D_l}{D_{\text{cl}}} \right) + V_{\odot,\text{pec}} \left( 1 - \frac{D_l}{D_{\text{cl}}} \right) \\ &= \begin{cases} (-260, -3) \pm (10, 9) \text{ km s}^{-1} \\ \text{or} \\ (-193, 54) \pm (10, 10) \text{ km s}^{-1} \end{cases}. \end{aligned} \quad (10)$$

These should be compared to the standard deviations for the disk velocities of  $\sigma_{\text{tot}}(l, b) = (30, 20) \text{ km s}^{-1}$ . Thus, in both cases the BD is significantly counter-rotating relative to the disk-stars' motion. Interestingly, one of these solutions is consistent, within small error bars, with perfectly planar counter-rotation. The other solution has considerable out-of-plane motion.

### 5.1. Constraints on Possible Distant Companion

Our data can rule out a distant companion to the BD via two channels. First, the flux from the companion cannot exceed the limits we found on the blend flux in Section 3.2.1 ( $I_b > 20.8$ ). We conservatively assume that the lensing system suffers the same extinction as the red clump ( $A_I \approx 2.7$ ) and use PARSEC-COLIBRI isochrones (Marigo et al. 2017) to calculate the brightness of possible companions at the distance of the BD. We find that the blend flux limit can exclude all main-sequence companions with  $M > 0.95 M_{\odot}$ .

The second constraint comes from the lack of additional features in the light curve. These features can be either anomalies in the apparent single-lens light curve (e.g., features due to caustics) or an additional point-lens-like event if the source passes near the companion (for more details, see Han et al. 2005). We follow the procedures of Mróz et al. (2018) and set a lower limit on the distance of a possible companion. In short, we simulated binary-lens light curves with a companion at a range of separations, with a range of masses and at all possible projected angles. We calculate the fraction of light curves that show additional features (using a threshold of  $\chi_{\text{single}}^2 - \chi_{\text{binary}}^2 > 60$ ) and consider a detection if 90% of the light curves pass this threshold. We find that companions with  $M = 0.95 M_{\odot}$  (the upper limit from lens flux) can be excluded for separations  $a_{\perp} < 65 \text{ au}$ , and companions with  $M = 0.08 M_{\odot}$  can be excluded for separations  $a_{\perp} < 20 \text{ au}$ .

The remaining parameter space of possible luminous companions (i.e., M/K dwarfs at separations  $a_{\perp} > 20 \text{ au}$ ) can be explored using future AO imaging, searching for any light from the putative companion (Gould 2016). This study can be done at first light of next generation (“30 m”) telescopes (perhaps 2028), as the lensing system will be separated by more than 50 mas from the source by then, and thus clearly resolved if luminous.

## 6. Discussion

We have presented the discovery of an  $\sim 19 M_J$  isolated BD, the lowest-mass isolated object ever measured. The BD is located at  $D_l \simeq 4 \text{ kpc}$  toward the Galactic bulge, but it is counter-rotating with respect to the kinematics of “normal” disk stars at this location. This is not the first example of a low-mass object with unusual kinematics. OGLE-2016-BLG-1195L (Shvartzvald et al. 2017) is a planetary system at  $D_l \simeq 4 \text{ kpc}$  with an Earth-mass planet orbiting an ultracool dwarf ( $\sim 0.08 M_{\odot}$ ), with significant west relative proper motion,  $\mu_{\text{hel,E}} \simeq -7.5 \text{ mas yr}^{-1}$ , although in that case the source proper motion was not measured and thus a fast moving source ( $\sim 360 \text{ km s}^{-1}$  relative to the bulge) is also possible. OGLE-2016-BLG-0864L (S.-J. Chung et al. 2018, in preparation) is a BD-BD binary system at  $D_l \simeq 3 \text{ kpc}$ , with relative proper motion suggesting the system is counter-rotating with respect to the disk motion (though, again, the source proper motion was not measured). In addition, while most local BDs have

similar kinematics as stars (e.g., Faherty et al. 2009), there is a growing sample of local BDs (Zhang et al. 2017) associated with kinematics of halo stars, including even a counter-rotating BD (Cushing et al. 2009).

The combined measurements of the satellite microlens parallax with *Spitzer* and the detection of finite-source effects enabled the full characterization of the BD properties accessible to microlensing (mass and five out of six phase-space coordinates). Microlensing is the only technique that can characterize the kinematics of low-mass dark objects throughout the Galaxy. This method can also be extended to free-floating planets (Gould 2016; Henderson & Shvartzvald 2016). A possible explanation of the kinematics of OGLE-2017-BLG-0896L is that it is a halo BD. Alternatively, it might suggest, along with the other examples mentioned above, the existence of a counter-rotating population of low-mass objects. Counter-rotating stellar disk populations have been detected in other galaxies (e.g., Rubin 1994; Pizzella et al. 2014; Armstrong & Bekki 2018), suggesting an occurrence rate of  $\sim 10\%$  for spirals and  $\sim 30\%$  for S0 galaxies (Pizzella et al. 2004). The scale of the counter-rotating component can range from a few tens of parsecs (e.g., Corsini et al. 2003) to a few kiloparsecs (e.g., Rubin 1994). While locally there is no evidence for a large counter-rotating population in our Galaxy, it may exist in the inner Galaxy.

The selection criteria of *Spitzer* events (Yee et al. 2015), with the 3–10 day lag before event selection and the beginning of *Spitzer* observations, is favoring the detection of these BDs, which have longer timescales than expected from “normal” disk star kinematics (e.g., OGLE-2017-BLG-0896L, OGLE-2016-BLG-1195L). In addition, counter-rotating lenses will peak later as seen from *Spitzer* than from Earth, thus increasing the chances for parallax measurement. This can be considered as a microlens-parallax “Malmquist bias,” because events that will peak earlier for *Spitzer* might already be at baseline by the time of first *Spitzer* observations and thus the parallax will not be measured. The bias is mostly relevant for short  $t_E$  events and faint high-magnification events. However, for events with typical timescale and peak magnification this bias should be small.

We thank D. Kirkpatrick for fruitful discussions about BDs. Work by Y.K.J. and A.G. was supported by AST-1516842 from the US NSF. I.G.S. and A.G. were supported by JPL grant 1500811. Work by C. Han was supported by the grant (2017R1A4A1015178) of the National Research Foundation of Korea. This work is based (in part) on observations made with the *Spitzer* Space Telescope, which is operated by the Jet Propulsion Laboratory, California Institute of Technology, under a contract with NASA. Support for this work was provided by NASA through an award issued by JPL/Caltech. This work was partially supported by NASA contract NNG16PJ32C. The OGLE project has received funding from the National Science Centre, Poland, grant MAESTRO 2014/14/A/ST9/00121 to AU. This research has made use of the KMTNet system operated by the Korea Astronomy and Space Science Institute (KASI) and the data were obtained at three host sites of CTIO in Chile, SAAO in South Africa, and SSO in Australia. Work by S.R. and S.S. was supported by INSF-95843339. P.L.-P. was supported by MINEDUC-UA project, code ANT 1656. The research has made use of data obtained at the Danish 1.54 m telescope at ESOs La Silla Observatory.

## ORCID iDs

Yossi Shvartzvald  <https://orcid.org/0000-0003-1525-5041>  
 Jennifer C. Yee  <https://orcid.org/0000-0001-9481-7123>  
 Jan Skowron  <https://orcid.org/0000-0002-2335-1730>  
 Sebastiano Calchi Novati  <https://orcid.org/0000-0002-7669-1069>  
 Sean Carey  <https://orcid.org/0000-0002-0221-6871>  
 B. Scott Gaudi  <https://orcid.org/0000-0003-0395-9869>  
 Calen B. Henderson  <https://orcid.org/0000-0001-8877-9060>  
 Wei Zhu  <https://orcid.org/0000-0003-4027-4711>  
 Etienne Bachelet  <https://orcid.org/0000-0002-6578-5078>  
 Richard W. Pogge  <https://orcid.org/0000-0003-1435-3053>  
 Rachel A. Street  <https://orcid.org/0000-0001-6279-0552>  
 Thiam-Guan Tan  <https://orcid.org/0000-0001-5603-6895>  
 Yiannis Tsapras  <https://orcid.org/0000-0001-8411-351X>  
 Paweł Pietrukowicz  <https://orcid.org/0000-0002-2339-5899>  
 Radosław Poleski  <https://orcid.org/0000-0002-9245-6368>  
 Szymon Kozłowski  <https://orcid.org/0000-0003-4084-880X>  
 Krzysztof Ulaczyk  <https://orcid.org/0000-0001-6364-408X>  
 Michael D. Albrow  <https://orcid.org/0000-0003-3316-4012>  
 Sun-Ju Chung  <https://orcid.org/0000-0001-6285-4528>  
 Cheongho Han  <https://orcid.org/0000-0002-2641-9964>  
 Kyu-Ha Hwang  <https://orcid.org/0000-0002-9241-4117>  
 Youn Kil Jung  <https://orcid.org/0000-0002-0314-6000>  
 Yoon-Hyun Ryu  <https://orcid.org/0000-0001-9823-2907>  
 In-Gu Shin  <https://orcid.org/0000-0002-4355-9838>  
 Weicheng Zang  <https://orcid.org/0000-0001-6000-3463>  
 Martin Dominik  <https://orcid.org/0000-0002-3202-0343>  
 Sedighe Sajadian  <https://orcid.org/0000-0002-2859-1071>  
 Daniel F. Evans  <https://orcid.org/0000-0002-5383-0919>  
 Yuri I. Fujii  <https://orcid.org/0000-0002-3648-0507>  
 Tobias C. Hinse  <https://orcid.org/0000-0001-8870-3146>  
 Sohrab Rahvar  <https://orcid.org/0000-0002-7084-5725>  
 Markus Rabus  <https://orcid.org/0000-0003-2935-7196>  
 Colin Snodgrass  <https://orcid.org/0000-0001-9328-2905>

## References

- Abe, F., Airey, C., Barnard, E., et al. 2013, *MNRAS*, 431, 2975  
 Alard, C., & Lupton, R. H. 1998, *ApJ*, 503, 325  
 Albrow, M. D., Horne, K., Bramich, D. M., et al. 2009, *MNRAS*, 397, 2099  
 Alcock, C., Allsman, R. A., Alves, D. R., et al. 2001, *Natur*, 414, 617  
 An, J. H., Albrow, M. D., Beaulieu, J.-P., et al. 2002, *ApJ*, 572, 521  
 Armstrong, B., & Bekki, K. 2018, *MNRAS*, 480, L141  
 Batista, V., Beaulieu, J.-P., Bennett, D. P., et al. 2015, *ApJ*, 808, 170  
 Bennett, D. P., Bhattacharya, A., Anderson, J., et al. 2015, *ApJ*, 808, 169  
 Bensby, T., Yee, J. C., Feltzing, S., et al. 2013, *A&A*, 549, A147  
 Bessell, M. S., & Brett, J. M. 1988, *PASP*, 100, 1134  
 Bramich, D. M., Vidrih, S., Wyrzykowski, L., et al. 2008, *MNRAS*, 386, 887  
 Calchi Novati, S., Gould, A., Udalski, A., et al. 2015a, *ApJ*, 804, 20  
 Calchi Novati, S., Gould, A., Yee, J. C., et al. 2015b, *ApJ*, 814, 92  
 Camarillo, T., Dredger, P., & Ratra, B. 2018, *ApS&S*, 363, 268  
 Chabrier, G. 2003, *PASP*, 115, 763  
 Chung, S.-J., Zhu, W., Udalski, A., et al. 2017, *ApJ*, 838, 154  
 Claret, A., & Bloemen, S. 2011, *A&A*, 529, A75  
 Corsini, E. M., Pizzella, A., Coccatto, L., & Bertola, F. 2003, *A&A*, 408, 873  
 Cushing, M. C., Looper, D., Burgasser, A. J., et al. 2009, *ApJ*, 696, 986  
 Evans, D. F., Southworth, J., Maxted, P. F. L., et al. 2016, *A&A*, 589, A58  
 Faherty, J. K., Burgasser, A. J., Cruz, K. L., et al. 2009, *AJ*, 137, 1  
 Gaia Collaboration, Brown, A. G. A., Vallenari, A., et al. 2018, *A&A*, 616, A1  
 Gould, A. 1994a, *ApJL*, 421, L71  
 Gould, A. 1994b, *ApJL*, 421, L75  
 Gould, A. 2016, *JKAS*, 49, 123  
 Gould, A., Carey, S., & Yee, J. 2013, Spitzer Proposal ID, 10036  
 Gould, A., Carey, S., & Yee, J. 2014, Spitzer Proposal ID, 11006  
 Gould, A., Carey, S., & Yee, J. 2016, Spitzer Proposal ID, 13005  
 Gould, A., Dong, S., Bennett, D. P., et al. 2010, *ApJ*, 710, 1800  
 Gould, A., & Loeb, A. 1992, *ApJ*, 396, 104  
 Gould, A., Yee, J., & Carey, S. 2015a, Spitzer Proposal ID, 12013  
 Gould, A., Yee, J., & Carey, S. 2015b, Spitzer Proposal ID, 12015  
 Gould, A., & Yee, J. C. 2012, *ApJL*, 755, L17  
 Gould, A., & Yee, J. C. 2014, *ApJ*, 784, 64  
 Griest, K., & Safizadeh, N. 1998, *ApJ*, 500, 37  
 Han, C., Gaudi, B. S., An, J. H., & Gould, A. 2005, *ApJ*, 618, 962  
 Henderson, C. B., & Shvartzvald, Y. 2016, *AJ*, 152, 96  
 Hog, E., Novikov, I. D., & Polnarev, A. G. 1995, *A&A*, 294, 287  
 Jiang, G., DePoy, D. L., Gal-Yam, A., et al. 2004, *ApJ*, 617, 1307  
 Kervella, P., Thévenin, F., Di Folco, E., & Ségransan, D. 2004, *A&A*, 426, 297  
 Kim, S.-L., Lee, C.-U., Park, B.-G., et al. 2016, *JKAS*, 49, 37  
 Kroupa, P. 2001, *MNRAS*, 322, 231  
 Marigo, P., Girardi, L., Bressan, A., et al. 2017, *ApJ*, 835, 77  
 Miyamoto, M., & Yoshii, Y. 1995, *AJ*, 110, 1427  
 Mróz, P., Ryu, Y.-H., Skowron, J., et al. 2018, *AJ*, 155, 121  
 Nataf, D. M., Gould, A., Fouqué, P., et al. 2013, *ApJ*, 769, 88  
 Paczyński, B. 1986, *ApJ*, 304, 1  
 Pizzella, A., Corsini, E. M., Vega Beltrán, J. C., & Bertola, F. 2004, *A&A*, 424, 447  
 Pizzella, A., Morelli, L., Corsini, E. M., et al. 2014, *A&A*, 570, A79  
 Refsdal, S. 1966, *MNRAS*, 134, 315  
 Rubin, V. C. 1994, *AJ*, 108, 456  
 Schechter, P. L., Mateo, M., & Saha, A. 1993, *PASP*, 105, 1342  
 Schönrich, R., Binney, J., & Dehnen, W. 2010, *MNRAS*, 403, 1829  
 Shin, I.-G., Udalski, A., Yee, J. C., et al. 2018, *ApJ*, 863, 23  
 Shvartzvald, Y., Yee, J. C., Calchi Novati, S., et al. 2017, *ApJL*, 840, L3  
 Simpson, T. 1740, *Essays on Several Curious and Useful Subjects: In Speculative and Mix'd Mathematick* (London: H. Woodfall)  
 Skottfelt, J., Bramich, D. M., Hundertmark, M., et al. 2015, *A&A*, 574, A54  
 Skowron, J., & Gould, A. 2012, arXiv:1203.1034  
 Udalski, A. 2003, *AcA*, 53, 291  
 Udalski, A., Szymanski, M., Kaluzny, J., et al. 1994, *AcA*, 44, 227  
 Udalski, A., Szymański, M. K., & Szymański, G. 2015, *AcA*, 65, 1  
 Walker, M. A. 1995, *ApJ*, 453, 37  
 Wozniak, P. R. 2000, *AcA*, 50, 421  
 Yee, J. C., Gould, A., Beichman, C., et al. 2015, *ApJ*, 810, 155  
 Zhang, Z. H., Pinfield, D. J., Gálvez-Ortiz, M. C., et al. 2017, *MNRAS*, 464, 3040  
 Zhu, W., Calchi Novati, S., Gould, A., et al. 2016, *ApJ*, 825, 60